

# Continuous/Discontinuous Galerkin Difference Discretizations of High-Order Differential Operators

J. W. Banks<sup>1</sup> • B. Brett Buckner<sup>1</sup> • T. Hagstrom<sup>2</sup>

Received: 15 December 2021 / Revised: 17 May 2022 / Accepted: 31 May 2022 /

Published online: 30 June 2022

© The Author(s), under exclusive licence to Springer Science+Business Media, LLC, part of Springer Nature 2022

#### Abstract

We develop continuous/discontinuous discretizations for high-order differential operators using the Galerkin Difference approach. Grid dispersion analyses are performed that indicate a nodal superconvergence in the  $\ell^2$  norm. A treatment of the boundary conditions is described that ultimately leads to moderate growth in the spectral radius of the operators with polynomial degree, and in general the norms of the Galerkin Difference differentiation operators are significantly smaller than those arising from standard elements. Lastly, we observe that with the use of the Galerkin Difference space, the standard penalty terms required for discretizing high-order operators are not needed. Numerical results confirm the conclusions of the analyses performed.

**Keywords** Difference methods · Galerkin methods · Interior penalty methods · Galerkin differences

## 1 Introduction

High order derivative operators play an important role in modeling a variety of physical phenomena, e.g. mechanical beams and plates [1], fluids [2, 3], optics [4], and solid mechanics [5]. The finite element discretization of such operators leads to challenges associated with the higher minimal regularity required by weak formulations. Researchers have pursued a number of different strategies to construct stable approximation schemes. A well-known example of a conforming element is the  $C^1$  Argyris element [6] for the biharmonic operator.

> B. Brett Buckner bbuckner94@gmail.com

T. Hagstrom thagstrom@smu.edu

- Department of Mathematical Sciences, Rensselaer Polytechnic Institute, Troy, NY 12180, USA
- Department of Mathematics, Southern Methodist University, PO Box 750156, Dallas, TX 75275-0156, USA



However, the generalization of conforming elements to higher order derivatives requires the construction of new and likely more complicated finite element spaces. A second approach is to used mixed elements, e.g. the biharmonic equation can be reduced to two second order equations as in [7, 8]. However, mixed finite element methods still require care so that the so-called inf-sup conditions are satisfied, as needed to guarantee convergence [8, 9]. Most relevant to the present work are nonconforming methods which require additional terms at element boundaries incorporating the influence of discontinuities in the derivatives. Examples include methods for fourth and sixth order elliptic boundary value problems based on  $C^0$  test and trial spaces [10, 11].

In this work, we develop methods for arbitrary even order spatial operators based on  $C^0$  Galerkin Difference basis functions. Although the spatial derivative approximations are applicable to elliptic and parabolic problems, we are particularly interested in applying the method to equations that support traveling wave solutions. In this case, as is well-known, higher order methods can be more efficient for challenging problems involving propagation over many wavelengths. We claim that the proposed Galerkin Difference methods have a number of distinct advantages relative to standard  $C^0$  elements for problems with high order derivatives. Most importantly, the norms of the discrete derivative operators grow mildly as the method order is increased, in sharp contrast the standard methods. In addition, we observe nodal superconvergence at roughly double the design order, in analogy with results obtained for local discontinuous Galerkin approximations to the biharmonic operator [12, 13] and for Galerkin Difference methods in other settings [14, 15]. Interestingly, as previously demonstrated for second-order wave equations in [15], interior penalty terms are not required to stabilize the method. This leads to a different and somewhat simpler weak formulation than used in [10, 11].

The structure of this manuscript is as follows. Section 2 reviews the construction of the  $C^0$ Galerkin Difference basis functions. Section 3 demonstrates the construction of approximations to arbitrary even order derivative operators. Fourier methods are employed to establish the stability and superconvergence of the schemes for problems in all space or with periodic boundary conditions. In Sect. 4 we describe the direct enforcement approach to implementing boundary conditions developed in [16] and demosntrate experimentally that the resulting discretizations are stable and that the spectral radii of the approximations do not grow too rapidly with approximation order. Finally, Sect. 5 uses the Euler-Bernoulli beam equation as a prototypical high order differential equation and discusses the application of the discretization, important implementation details, and numerical results.

#### 2 Galerkin Difference Basis Functions

Similar to some prior Galerkin Difference discretizations, the construction used here is based on the space of piecewise continuous polynomial interpolants defined on a grid [14, 16–18]. Unlike prior work in continuous GD, however, the space here is non-conforming due to insufficient smoothness in derivatives of the interpolant. To fully understand the method, it is therefore appropriate to briefly review the derivation of the  $C^0$  Galerkin Difference basis functions. The discussion follows that of [14]. On an interval (a, b) let  $x_k = a + kh$  where h = (b - a)/N is the mesh size. Galerkin Difference functions associated with this mesh are certain continuous piecewise degree-p polynomials which we will denote by  $u^h$  and which are defined via an interpolation procedure. The basis functions are the result of using Lagrange interpolation to represent an element of the Galerkin Difference space. For the



piecewise degree p Galerkin Difference functions, set p=2q-1 and take the 2q-point stencil  $x_{k-q+1}, \ldots, x_{k+q}$ . The representation of  $u^h$  on the interval  $I_{k+1/2}=[x_k, x_{k+1}]$  is then given by

$$u^{h}(x) = \sum_{j=k-q+1}^{k+q} u_{j} \mathcal{L}_{k,j}(x),$$
 (1)

where  $\mathcal{L}_{k,j}(x)$  is the Lagrange basis function

$$\mathcal{L}_{k,j}(x) = \prod_{\substack{k-q+1 \le m \le k+q \\ m \ne j}} \frac{x - x_m}{x_j - x_m}.$$
 (2)

Each coefficient  $u_j$  then contributes to (i.e. is a coefficient in) the interpolation performed on 2q consecutive intervals, and determining the contribution of each coefficient can be viewed as computing the basis function corresponding to that coefficient. Thus, we may associate a basis function of width 2q (corresponding to its radius of contribution) to each  $x_j$ . Moreover, on a uniform grid these basis functions are obviously translation invariant. For example, the basis function for p=3 is

$$\phi_{j}^{(3)}(\xi_{j}) = \begin{cases} \frac{(\xi_{j} + 3h)(\xi_{j} + 2h)(\xi_{j} + h)}{6h^{3}} & -2h < \xi_{j} \leq -h \\ -\frac{(\xi_{j} + 2h)(\xi_{j} + h)(\xi_{j} - h)}{2h^{3}} & -h < \xi_{j} \leq 0 \\ \frac{(\xi_{j} + h)(\xi_{j} - h)(\xi_{j} - 2h)}{2h^{3}} & 0 < \xi_{j} \leq h \\ -\frac{(\xi_{j} - h)(\xi_{j} - 2h)(\xi_{j} - 3h)}{6h^{3}} & h < \xi_{j} \leq 2h \\ 0 & \text{else} \end{cases}$$
(3)

where  $\xi_j = x - x_j$  and  $x_j$  is the center of the basis function. Similarly, the basis function for p = 5 is

$$\phi_{j}^{(5)}(\xi_{j}) = \begin{cases} \frac{(\xi_{j} + 5h)(\xi_{j} + 4h)(\xi_{j} + 3h)(\xi_{j} + 2h)(\xi_{j} + h)}{120h^{5}} & -3h < \xi_{j} \leq -2h \\ -\frac{(\xi_{j} + 4h)(\xi_{j} + 3h)(\xi_{j} + 2h)(\xi_{j} + h)(\xi_{j} - h)}{24h^{5}} & -2h < \xi_{j} \leq -h \\ \frac{(\xi_{j} + 3h)(\xi_{j} + 2h)(\xi_{j} + h)(\xi_{j} - 2h)}{12h^{5}} & -h < \xi_{j} \leq 0 \\ -\frac{(\xi_{j} + 2h)(\xi_{j} + h)(\xi_{j} - h)(\xi_{j} - 2h)(\xi_{j} - 3h)}{12h^{5}} & 0 < \xi_{j} \leq h \\ \frac{(\xi_{j} + h)(\xi_{j} - h)(\xi_{j} - 2h)(\xi_{j} - 3h)(\xi_{j} - 4h)}{24h^{5}} & h < \xi_{j} \leq 2h \\ -\frac{(\xi_{j} - h)(\xi_{j} - 2h)(\xi_{j} - 3h)(\xi_{j} - 4h)(\xi_{j} - 5h)}{120h^{5}} & 2h < \xi_{j} \leq 3h \\ 0 & \text{else.} \end{cases}$$

Basis functions for various values of p are plotted in Fig. 1, and there are a number of interesting properties to note. The basis functions decay rapidly away from  $\xi_j = 0$ , and as a result the off-diagonal elements of the mass and stiffness matrices will also decay rapidly. Of particular interest in what follows, although the derivatives of these basis functions contain singularities at element interfaces (e.g. discontinuities in the first derivative), the left and right limits of the derivatives are well-defined. At element interfaces, these left and right limits differ for all odd-order derivatives, but interestingly they are equal for all even-order derivatives (including the undifferentiated basis itself which is continuous). The short argument establishing this fact is given in the Proof of Lemma 1.



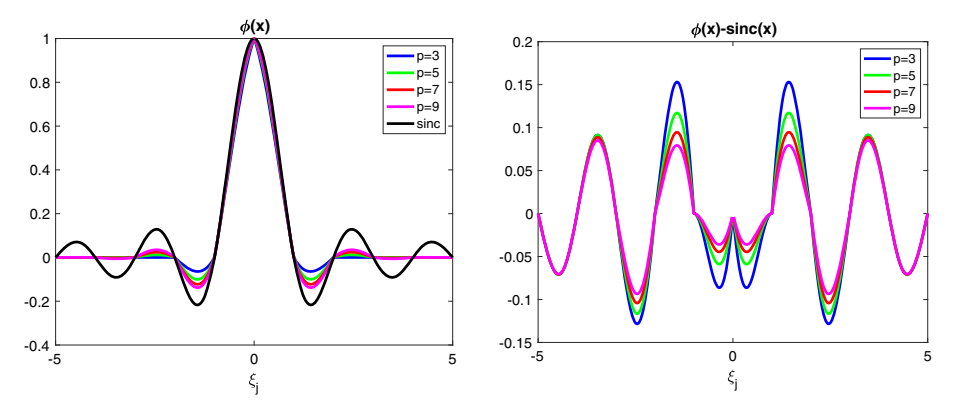


Fig. 1 At left are plots of the  $C^0$  Galerkin Difference basis functions for p = 3, 5, 7, 9, along with the since function that is the limit as  $p \to \infty$ . The right plot shows the difference between sinc and the various basis functions

## 3 Discretization of High Order Derivatives

Because the basis described in Sect. 2 spans a subspace of  $C^0$ , we are motivated to pursue an interior penalty method for higher-order derivative approximation as proposed for elliptic problems using standard elements in [10, 11]. To simplify the presentation, rather than beginning with time-dependent PDEs in multiple space dimensions, consider the simple ODE given by

$$\frac{\partial^{2m}}{\partial x^{2m}}u = w, (5)$$

defined over some  $\Omega = (a, b)$ , with suitable boundary conditions imposed at the endpoints of the interval x = a, b. For notational convenience, we will use the convention that  $\frac{\partial^{2m}}{\partial x^{2m}}u$  can be expressed as  $\partial^{2m}u$ , and for cases with a fixed integer derivative we may also use subscripts to indicate derivatives, e.g.  $\partial^3 u = u_{xxx}$ . The assumption of even order in (5) is taken so that resulting discrete operator can easily be made adjoint consistent, which is apparently important for recovering the superconvergence often observed with Galerkin Difference methods. Nevertheless, extensions to odd-order derivatives may be pursued using the ideas from [19]. Note that the simplifying assumptions of time independence and 1D are made for purely pedagogical reasons. Application to time dependent problems will be described in Sect. 5, and will use a standard method-of-lines technique with a spectral-deferred correction time integrator. Higher dimensional problems will also be described in Sect. 5 and will use a tensor-product construction similar to previous work on Galerkin Differences, e.g. [15, 17]. The remainder of this section is dedicated to defining the  $C^0$  Galerkin Difference discretization of Eq. (5), and analyzing its stability properties. A dispersion analysis will be performed for various derivative orders demonstrating that, away from the boundaries, the scheme exhibits superconvergence. In addition we note the uniform boundedness of the spectrum of the derivative operators with increasing degree p. This is in sharp contrast with standard finite elements where the spectral radius grows rapidly with degree.



## 3.1 Symmetric C<sup>0</sup> Galerkin Difference Method

In what follows, the standard definitions of the one dimensional jump  $[\cdot]$  and average  $\{\cdot\}$  operators are adopted, as in [20], and given by

$$[v] = v(x^{+}) - v(x^{-}), \quad \{\{v\}\} = \frac{1}{2} \left( v(x^{+}) + v(x^{-}) \right), \quad (6)$$

where  $v(x^+) = \lim_{\epsilon \to 0, \ \epsilon > 0} v(x + \epsilon)$ , and  $v(x^-) = \lim_{\epsilon \to 0, \ \epsilon > 0} v(x - \epsilon)$ . As mentioned above, for Galerkin Difference basis functions there is no jump in even derivatives across element boundaries, and so any jump terms involving those derivatives will vanish. For now the imposition of boundary conditions is neglected, with relevant discussion delayed until Sect. 4.1.

Derivation of the weak form now follows the standard procedure. First, assuming a smooth solution u, Eq. (5) is multiplied by a test function  $\phi$  which is continuous and piecewise smooth on the grid. Integration over the domain then gives

$$\int_{\Omega} \phi \partial^{2m} u \, dx = \int_{\Omega} \phi w \, dx. \tag{7}$$

Recalling the notation  $I_{k+1/2} = (x_k, x_{k+1})$  for the elements, the integral is rewritten as a sum over elements, and integration by parts is applied m times in each element, where  $\phi$  is smooth over each interval. With this approach, the boundary terms at a node  $x_k$  are given by

$$-\sum_{j=1}^{m-1} (-1)^{j} \partial^{\bar{j}} u \left[ \partial^{j} \phi \right], \quad \bar{j} = 2m - j - 1.$$
 (8)

Since u is assumed to be smooth, its value can be replaced by its average. The boundary terms can then be symmetrized by adding terms proportional to the jumps of derivatives of u, which vanish for smooth solutions, leading to

$$-\sum_{j=1}^{m-1} (-1)^j \left[ \left\{ \left\{ \partial^{\bar{j}} u \right\} \right\} \left[ \left[ \partial^j \phi \right] \right] + \left[ \left[ \partial^j u \right] \right] \left\{ \left\{ \partial^{\bar{j}} \phi \right\} \right\} \right]. \tag{9}$$

This process yields a well-defined bilinear form in the broken Sobolev space consisting of functions in  $H^1$  whose restriction to each element are in  $H^s$ , s > 2m - 1/2. Specializing to the Galerkin Difference space, and exploiting the fact, demonstrated in the Proof of Lemma 1, that the jumps of all even derivative terms vanish yields the Galerkin approximation

$$\int_{\Omega} \phi^{h} w \, dx = (-1)^{m} \sum_{k} \int_{I_{k+1/2}} \partial^{m} u^{h} \, \partial^{m} \phi^{h} \, dx 
+ \sum_{k} \sum_{j=1}^{\lfloor m/2 \rfloor} \left[ \left\{ \left\{ \partial^{2(m-j)} u^{h} \right\} \right\} \left[ \left[ \partial^{2j-1} \phi^{h} \right] \right] + \left[ \left[ \partial^{2j-1} u^{h} \right] \right] \left\{ \left\{ \partial^{2(m-j)} \phi^{h} \right\} \right\} \right]_{x=x_{k}},$$
(10)

where  $\lfloor m/2 \rfloor$  denotes the integer part of m/2. Note that continuity of even derivatives for functions in the GD space implies that any averaging operators in (10) take two identical arguments, although the notation is retained for clarity. We hypothesize that for a uniform grid this discretization has a nodal truncation error  $\mathcal{O}(h^{2p+2-2m})$ . This would imply that for all-space or periodic problems the method when combined with an appropriate time-stepping scheme would exhibit convergence at the superconvergent rate of  $\mathcal{O}(h^{2p+2-2m})$  in



the  $\ell^2$  norm.<sup>1</sup> See, for example, Theorem 10.1.4 in [21]. This prediction is supported by the dispersion analyses which is presented below. Further, this observed rate is a generalization of those found in [14, 15, 19]. For finite domain problems, boundary closures (discussed in Sect. 4.1) will lower the convergence rate, though the high-order local truncation error of the method will be beneficial for improving accuracy.

## 3.2 Positivity of the Bilinear Form

In contrast to the usual interior penalty methods, we find that no additional penalty terms beyond those arising in the integration by parts, and any symmetrizing terms, need to be introduced to guarantee positivity of the bilinear form. Ignoring boundary closures this fact can be proved using Fourier techniques; we demonstrate experimentally in Sect. 4.1 that they are still not needed in the presence of boundaries using the closures we propose. Consider the problem posed on  $\mathbb{R}$ , although one could alternately consider a finite periodic domain with u(x + (b - a)) = u(x) (see Remark 1). Suppose that  $u^h$  is in the Galerkin Difference space and decays rapidly enough so that  $u^h \in L^2$ . Positivity of the discrete bilinear form follows from the following theorem.

**Theorem 1** Let  $u^h \in L^2(\mathbb{R})$  be a degree p Galerkin Difference function associated with a uniform mesh in  $\mathbb{R}$  with h > 0, and suppose  $m \leq \frac{p+1}{2}$ . Then

$$\sum_{k=-\infty}^{\infty} \int_{I_{k+1/2}} \left( D^m u^h \right)^2 dx + 2(-1)^m \sum_{k=-\infty}^{\infty} \sum_{j=1}^{\lfloor m/2 \rfloor} \left[ \left\{ \left\{ \partial^{2(m-j)} u^h \right\} \right\} \left[ \left[ \partial^{2j-1} u^h \right] \right]_{x=x_k} > 0.$$
 (11)

**Proof** Obviously the terms involving integrals over the elements are nonnegative. Therefore consider the jump terms. As described, for example, in [21], grid functions can be represented by bandlimited Fourier transforms and  $\ell^2$  inner products computed in terms of these transforms by Parseval's lemma. Thus

$$(-1)^{m} \sum_{k=-\infty}^{\infty} \left[ \left\{ \left\{ \partial^{2(m-j)} u^{h} \right\} \right\} \left[ \left[ \partial^{2j-1} u^{h} \right] \right]_{x=x_{k}} \right.$$

$$= \frac{(-1)^{m}}{2\pi h} \int_{-\pi/h}^{\pi/h} \hat{\rho}_{2(m-j)}(\xi) \hat{\zeta}_{2j-1}(\xi) |\hat{u}(\xi)|^{2} d\xi, \tag{12}$$

where the real-valued functions  $\hat{\rho}_{2(m-j)}$  and  $\hat{\zeta}_{2j-1}$  are the symbols of the difference operators which produce, respectively,  $\{\{\partial^{2(m-j)}u^h\}\}$  and  $[\![\partial^{2j-1}u^h]\!]$  on the grid and  $\hat{u}$  is the Discrete Fourier transform of the grid function defined by the values of  $u^h$  on the grid. Note this is not the Fourier transform of the Galerkin Difference function  $u^h$ . That the form is nonnegative then follows from Lemma 1 shown below. To establish positivity we note that for the form to be zero,  $u^h$  restricted to each element would need to be a polynomial of degree less than m. However, for  $p \geq 2m-1$ , a simple argument shows that such an element of the Galerkin Difference space must be a global polynomial of degree less than m. In particular, given a particular element  $I_{k+1/2}$ , the polynomial of degree less than m-1 in its neighboring

We use the convention that  $\ell^2$  denotes the discrete-  $L^2$  norm.



elements  $I_{k-1/2}$ ,  $I_{k+3/2}$ , will be uniquely defined by the data in their common interpolation stencils with  $I_{k+1/2}$ . Since global polynomials are not elements of  $L^2(\mathbb{R})$  the result is established.

**Remark 1** In the periodic case the form will be zero for constant functions, but positive otherwise.

**Lemma 1** The symbols  $\hat{\rho}_{2(m-j)}$  and  $\hat{\zeta}_{2j-1}$ ,  $j=1,\ldots,\lfloor m/2\rfloor$  are real and satisfy

$$(-1)^m \hat{\rho}_{2(m-j)} \hat{\zeta}_{2j-1} \ge 0. \tag{13}$$

**Proof** To prove the result, the average of the even derivatives and jump of the odd derivatives will be represented using standard finite difference operators  $D_0$ ,  $D_+$  and  $D_-$ . We first show that there are no jumps in the even derivatives of the Galerkin difference functions at a node  $x_k$ . To do so, express the interpolants on intervals  $(x_{k-1}, x_k)$  and  $(x_k, x_{k+1})$  in Newton form, respectively as  $Q_k(x) + c_L R_k(x)$ , and  $Q_k(x) + c_R R_k(x)$  with  $R_k(x) = \prod_{m=k-q+1}^{k+q-1} (x-x_m)$  and  $Q_k(x)$  the degree p-1=2q-2 interpolant of the data at the nodes  $(x_{k-q+1}, \ldots, x_{k+q-1})$ . Since  $R_k(x)$  is odd with respect to  $x_k$ , all of its even derivatives vanish at  $x_k$  and so the left and right limits of these derivatives agree. These derivatives are thus simply the maximal order central difference approximation using the p-point stencil extending from  $x_{k-(p-1)/2}$  to  $x_{k+(p-1)/2}$ . Dropping the index k for notational simplicity, the average of even derivatives can thus be written

$$(-1)^{r} \left\{ \left\{ \partial^{2r} u^{h} \right\} \right\} = (-1)^{r} \left( D_{+} D_{-} \right)^{r} \sum_{i=0}^{\frac{p-1}{2} - r} \alpha_{r,j} \left( h^{2} D_{+} D_{-} \right)^{j} u^{h}. \tag{14}$$

for r a positive integer. To compute the coefficients  $\alpha_{r,j}$ , and ultimately the symbol  $\hat{\rho}_{2r}$ , recall that

$$D_{+}D_{-}e^{i\xi x} = -\frac{4}{h^{2}}\sin^{2}\eta e^{i\xi x}, \quad \eta = \xi h/2.$$
 (15)

Setting  $z = \sin \eta$  so that  $\xi = \frac{2}{h} \arcsin z$ , the symbol of the difference formula (14) maximizes the order of approximation to  $\xi^{2r}$ , and so

$$\frac{4^r}{h^{2r}}(\arcsin z)^{2r} + O(z^{p+1}) = \frac{4^r}{h^{2r}}z^{2r} \sum_{j=0}^{\frac{p-1}{2}-r} \alpha_{r,j}(-1)^j 4^j z^{2j}.$$
 (16)

Now recall the Maclaurin series expansion for arcsin z, which gives

$$\xi = \frac{2}{h}\arcsin z = \frac{2}{h}\sum_{n=0}^{\infty} \frac{(2n-1)!!}{(2n)!!} \frac{z^{2n+1}}{2n+1}.$$
 (17)

The essential features of this series which will be used are that only odd powers of z appear, and all coefficients multiplying powers of z are positive. Substituting this expansion into (16) the gives

$$\frac{4^r}{h^{2r}} \left( \sum_{n=0}^{\frac{p-1}{2}-r} \frac{(2n-1)!!}{(2n)!!} \frac{z^{2n+1}}{2n+1} \right)^{2r} + O(z^{p+1}) = \frac{4^r}{h^{2r}} z^{2r} \sum_{j=0}^{\frac{p-1}{2}-r} \alpha_{r,j} (-1)^j 4^j z^{2j}.$$
(18)



Since all terms on the left-hand-side of (18) have positive coefficients, all terms on the righthand-side must also have positive coefficients and so  $\alpha_{r,j}(-1)^j > 0$ . Thus

$$(-1)^r \hat{\rho}_{2r} = \frac{4^r}{h^{2r}} z^{2r} \sum_{j=0}^{\frac{p-1}{2}-r} \alpha_{r,j} (-1)^j 4^j z^{2j} \ge 0.$$
 (19)

Now consider the jump in an odd derivative  $[\partial^{2j-1}u^h]$ . The left and right limits can be written as corrections to the central difference approximation on the p-point stencil, which has the form

$$D_{2j-1,\text{central}} = D_0 (D_+ D_-)^{j-1} \sum_{i=0}^{\frac{p-1}{2}-j} \beta_{j,j} (h^2 D_+ D_-)^j.$$
 (20)

Similar to above, the coefficients  $\beta_{i,j}$  are computed by considering the symbols in Fourier space. To that end recall

$$D_0 e^{i\xi x} = i\frac{2}{h}\cos\eta \cdot \sin\eta e^{i\xi x} = i\frac{2}{h}\sqrt{1-z^2}ze^{i\xi}.$$

Maximizing the order of approximation in (20) to  $(i\xi)^{2j-1}$  then leads to

$$i(-1)^{j-1} \frac{2^{2j-1}}{h^{2j-1}} (\arcsin z)^{2j-1} + O(z^p)$$

$$= i(-1)^{j-1} \frac{2^{2j-1}}{h^{2j-1}} z^{2j-1} \sqrt{1-z^2} \sum_{j=0}^{\frac{p-1}{2}-j} \beta_{j,j} (-1)^j 4^j z^{2j}. \tag{21}$$

Cancelling like terms and using the fact that  $\sqrt{1-z^2} = O(1)$  for  $z \ll 1$  yields

$$\frac{(\arcsin z)^{2j-1}}{\sqrt{1-z^2}} + O(z^p) = z^{2j-1} \sum_{i=0}^{\frac{p-1}{2}-j} \beta_{j,j} (-1)^j 4^j z^{2j}.$$
 (22)

Because the expansion (17) for  $\arcsin z$ , as well as the expansion for  $1/\sqrt{1-z^2}$ 

$$\frac{1}{\sqrt{1-z^2}} = \sum_{n=0}^{\infty} \frac{(2n-1)!!}{2^n n!} z^{2n}$$
 (23)

contains strictly positive coefficients, the terms on the right-hand-side of (22) must also have positive coefficients. Therefore  $\beta_{i,j}(-1)^j > 0$ .

Now the left and right approximations to the derivative can be written as the central approximation (20) plus a one-sided approximation to the first missing term in the expansion of the central difference formula:

$$h^{p+1-2j}\beta_{j,\frac{p+1}{2}-j}\partial^p$$
.

Therefore the difference formulas from the right (+ sign) and left (- sign) are

$$D_{2j-1,\text{central}} + h^{p+1-2j} \beta_{j,\frac{p+1}{2}-j} D_{\pm} (D_+ D_-)^{\frac{p+1}{2}-j}.$$

Since  $D_+ - D_- = hD_+D_-$ , the jump is given by

$$h^{p+2-2j}\beta_{j,\frac{p+1}{2}-j}(D_+D_-)^{\frac{p+1}{2}},$$



and its symbol is

$$(-1)^{j}\hat{\zeta}_{2j-1} = (-1)^{\frac{p+1}{2}-j}\beta_{j,\frac{p+1}{2}-j}\frac{4^{\frac{p+1}{2}}}{h^{2j-1}}z^{p+1} \ge 0.$$
 (24)

Finally using (19) and (24) together implies

$$(-1)^{m} \hat{\rho}_{2(m-j)} \hat{\zeta}_{2j-1} = \left( (-1)^{m-j} \hat{\rho}_{2(m-j)} \right) \left( (-1)^{j} \hat{\zeta}_{2j-1} \right) \ge 0.$$
 (25)

This completes the proof.

## 3.3 Dispersion Analysis

The Fourier methods used above also enable the analysis of the dispersion errors of the method away from boundaries. Suppose that the coefficients in the mass, stiffness, and lift matrices for the GD discretization (10) based on p-th degree polynomial interpolation are given by  $M_{\gamma}^{(p)}$ ,  $K_{\gamma}^{(2m,p)}$ , and  $F_{\gamma}^{(2m,p)}$  for  $\gamma = -p \dots p$ , respectively. Then the action of the operator  $(M^{(p)})^{-1}(K^{(2m,p)}+F^{(2m,p)})$  on a grid function  $u_j = \exp(i\xi x_j)$  yields the Fourier symbol of the Galerkin Difference approximation to the 2m-th derivative,

$$(i\xi)^{2m} \approx \frac{\sum_{\gamma=-p}^{p} \left( K_{\gamma}^{(2m,p)} + F_{\gamma}^{(2m,p)} \right) \exp(i\gamma\eta)}{\sum_{\gamma=-p}^{p} M_{\gamma}^{(p)} \exp(i\gamma\eta)} \equiv \frac{1}{h^{2m}} \mathcal{S}^{(2m,p)}(\eta)$$
(26)

where  $\xi$  is a physical wave number,  $\eta = \xi h$  is a grid wave number, and  $\mathcal{S}^{(2m,p)}$  is used to denote the symbol of the 2m-th derivative approximation in (10) using degree p basis functions.

## 3.3.1 Biharmonic Operator

Consider the previously defined variational form (10) as an approximation of the fourth derivative. For the sake of clarity this can be expressed as

$$\int_{\Omega} u_{xxxx} \phi^h dx \approx \sum_{k} \int_{I_{k+1/2}} u_{xx}^h \phi_{xx}^h dx + \sum_{k} \left[ \left\{ \left\{ u_{xx}^h \right\} \right\} \left[ \left[ \phi_x^h \right] \right] + \left[ \left[ u_x^h \right] \right] \left\{ \left\{ \phi_{xx}^h \right\} \right\} \right]_{x=x_k},$$
(27)

Note here that to ensure consistency of the operator, p > 3 is assumed.

Values for the coefficients of the mass, stiffness, and lift matrices are given in Table 1, and the symbols for various polynomial degrees are as follows:

$$S^{(4,3)} = \eta^4 + \frac{1}{720}\eta^8 + \frac{19}{15120}\eta^{10} + O\left(\eta^{12}\right)$$

$$S^{(4,5)} = \eta^4 + \frac{41}{86400}\eta^{12} - \frac{1847}{15966720}\eta^{14} + O\left(\eta^{16}\right)$$

$$S^{(4,7)} = \eta^4 + \frac{4609559}{145297152000}\eta^{16} - \frac{54385141}{3923023104000}\eta^{18} + O\left(\eta^{20}\right)$$

$$S^{(4,9)} = \eta^4 + \frac{1357881299}{727542466560000}\eta^{20} - \frac{5796689608471}{5109094217170944000}\eta^{22} + O\left(\eta^{24}\right).$$
(28)

As mentioned above, these symbols indicate superconvergence at the rate of 2p - 2 for the infinite domain problem, in agreement with a general superconvergent rate 2p + 2 - 2m.



Table 1 Coefficients for the mass, stiffness, and lift matrices at interior grid points for the symmetric interior penalty approximation to the fourth derivative (27) with p = 3

γ	0	±1	±2	±3
$M_{\gamma}^{(3)}$	733h 945	$\frac{257h}{1680}$	$-\frac{3h}{70}$	31 15120
$K_{\gamma}^{(4,3)}$	$\frac{8}{3h^3}$	$-\frac{3}{2h^3}$	0	$\frac{1}{6h^3}$
$F_{\gamma}^{(4,3)}$	$\frac{20}{3h^3}$	$-\frac{5}{h^3}$	$\frac{2}{h^3}$	$-\frac{1}{3h^3}$

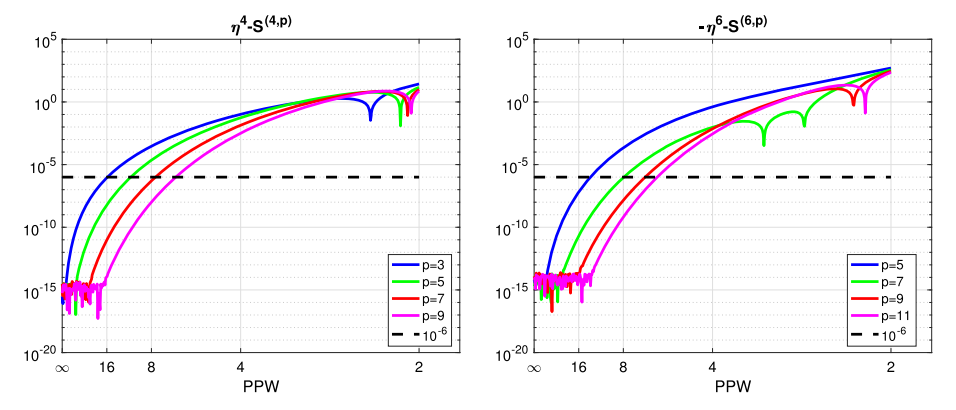


Fig. 2 Errors in the symbols for the fourth (left) and sixth (right) derivatives. A reference line indicating an error of 10<sup>-6</sup> is displayed for convenience

Of note (and not presented here) is that when the inter-elemental jump terms from the integration by parts are excluded, the expected order of accuracy according to the dispersion analysis becomes p-1, which is consistent with the error estimates and computations present in [22]. The same is true if the jump terms are included but the symmetrizing terms are excluded. Hence, the symmetrization is seen to lead to a nodal superconvergence at double the asymptotic order. In addition, the discrete symbols are pure real and positive. Figure 2 displays the errors in the symbols, plotted as functions of the number of points per wavelength  $(PPW = \frac{2\pi}{n})$ . This shows that, neglecting the treatment of the boundary conditions, as few as 16 points per wavelength are required to achieve machine precision accuracy for the 4th derivative using p = 9, and approximately 7 points is sufficient to achieve a tolerance of  $10^{-6}$ .

We also emphasize the favorable behavior of the derivative approximations as a function of p. As shown in Fig. 3, the eigenvalues of the Galerkin Difference approximations, which in the periodic case lie on the plotted curves, never exceed  $\pi^4 h^{-4}$ . Experiments with even larger values of p show that this feature is apparently retained for all p. In contrast, one expects the eigenvalues of standard finite element approximations for fourth derivative operators to scale like  $p^8$ . Comparing methods with the same average grid density, that is setting the element width H = ph to compare with the present GD methods on a grid spacing of h, one expects the spectral radius (and the norm) of the standard finite element operators to grow in proportion to  $p^4h^{-4}$ . This is verified in Table 2, which presents the spectral radii of the more standard finite element approach proposed in [10]. Precisely, the scheme uses Gauss-Lobatto nodes and mass lumping, and results are presented for the smallest penalty parameter for which the spatial operator remains definite. The fourth order growth with p is clearly observed. Furthermore, for large p the spectral radius of the operators resulting from



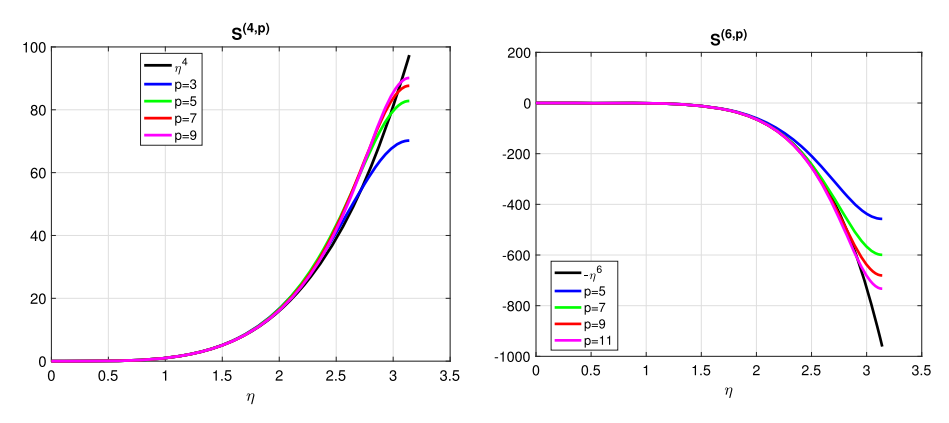


Fig. 3 Symbols for the fourth (left) and sixth (right) derivatives compared with the exact symbol

**Table 2** Computed spectral radius  $\rho_{FEM}$  as a function of p for standard SIPGD approximations to the fourth derivative with periodic boundary conditions and Gauss-Lobatto nodes.

p	5	7	9	11	13
$\rho_{FEM}$	$4.6 \times 10^{2}$	$2.0 \times 10^{3}$	$5.4 \times 10^{3}$	$1.3 \times 10^{4}$	$2.5 \times 10^4$
$ ho_{GD}$	$8.3 \times 10^{1}$	$8.8 \times 10^{1}$	$9.0\times10^{1}$	$9.2 \times 10^{1}$	$9.3\times10^{1}$
$ ho_{FEM}/\pi^4$	$4.8 \times 10^{0}$	$2.1 \times 10^{1}$	$5.6 \times 10^{1}$	$1.3 \times 10^2$	$2.6\times10^2$
$ ho_{FEM}/ ho_{GD}$	$5.6 \times 10^{0}$	$2.3 \times 10^{1}$	$6.2 \times 10^{1}$	$1.4 \times 10^2$	$2.7\times10^2$

Here the element widths are H=p so the methods have the same grid average grid density as Galerkin Difference discretizations with h=1. The ratio  $\rho_{FEM}/\pi^4$  illustrates the growth in the spectral radius of the standard SIPGD scheme in relation to the continuous limit  $\pi^4$  (i.e. the Fourier derivative with two points per wavelength). Also included is the spectral radius of the GD method with periodic boundary conditions,  $\rho_{GD}$ . The ratio  $\rho_{FEM}/\rho_{GD}$  illustrates the improvement in spectral radius for GD vs. the standard SIPGD scheme

standard finite elements are observed to be orders of magnitude larger than the exact value  $\pi^4$  and the corresponding GD scheme.

#### 3.3.2 Sixth Order Operator

Consider now the variational form (10) as an approximation of the sixth derivative, which can be expressed as

$$\int_{\Omega} \partial^{6} u \phi^{h} dx \approx -\sum_{k} \int_{I_{k+1/2}} u_{xxx}^{h} \phi_{xxx}^{h} dx 
+ \sum_{k} \left[ \left\{ \left\{ u_{xxxx}^{h} \right\} \right\} \left[ \left[ \phi_{x}^{h} \right] \right] + \left[ \left[ u_{x}^{h} \right] \right] \left\{ \left\{ \phi_{xxxx}^{h} \right\} \right\} \right]_{x=x_{k}}.$$
(29)

Here assume for consistency that  $p \ge 5$ . Table 3 shows values for the coefficients in the mass, stiffness, and lift matrices. Furthermore, the symbols of the operators, again defined



γ	0	±1	±2	±3	±4	±5
$M_{\gamma}^{(5)}$	455963 <i>h</i> 554400	906919h 6652800	$-\frac{12421h}{207900}$	59053 <i>h</i> 4435200	$-\frac{3937h}{3326400}$	313 <i>h</i> 4435200
$K_{\gamma}^{(6,5)}$	$-\frac{687}{20h^5}$	$\frac{211}{8h^5}$	$-\frac{23}{2h^5}$	$\frac{39}{16h^5}$	$-\frac{1}{8h^5}$	$-\frac{1}{80h^5}$
$F_{\gamma}^{(6,5)}$	$-\frac{84}{5h^5}$	$\frac{14}{h^5}$	$-\frac{8}{h^5}$	$\frac{3}{h^5}$	$-\frac{2}{3h^5}$	$\frac{1}{15h^5}$

**Table 3** Coefficients for the interior grid points for the mass, stiffness, and lift matrices for the interior penalty approximation to the sixth derivative for p = 5

in (26), are as follows:

$$S^{(6,5)} = -\eta^6 + \frac{313}{60480}\eta^{12} - \frac{443}{201600}\eta^{14} + O\left(\eta^{16}\right)$$

$$S^{(6,7)} = -\eta^6 + \frac{1889}{26611200}\eta^{16} - \frac{68510773}{1307674368000}\eta^{18} + O\left(\eta^{20}\right)$$

$$S^{(6,9)} = -\eta^6 - \frac{91201}{40758681600}\eta^{20} + \frac{1114437953}{1600593426432000}\eta^{22} + O\left(\eta^{24}\right)$$

$$S^{(6,11)} = -\eta^6 - \frac{64808934653}{196503623737344000}\eta^{24} + \frac{86736626469487}{374666909259202560000}\eta^{26} + O\left(\eta^{28}\right).$$
(30)

These symbols reveal superconvergence of the truncation error at order 2p - 4, again in agreement with a general superconvergent rate 2p + 2 - 2m. Similar to the case of the 4th derivative, we note that without the symmetrizing terms the truncation error converges with order p-1. Furthermore, the symbols here are seen to be pure real and negative. Finally, Fig. 2 shows the errors in the symbols, plotted as functions of the number of points per wavelength  $(PPW = \frac{2\pi}{n})$ . This shows that neglecting the treatment of the boundary conditions, as few as 10 points per wavelength are required to achieve machine precision accuracy for the sixth derivative using p = 11, and approximately 6 points is sufficient to achieve a tolerance of  $10^{-6}$ .

We again emphasize the favorable behavior of the GD derivative approximations as a function of p. As shown in Fig. 3, the eigenvalues of the Galerkin Difference approximations never exceed  $\pi^6 h^{-6}$ . In contrast, one expects the sixth order derivative operators for standard finite element approximations to scale like  $p^{12}$ . A before, comparing methods with the same average grid density, that is setting the element width H = ph to compare with our methods and a grid spacing of h, one expects the spectral radius (and the norm) of the standard finite element operators to grow in proportion to  $p^6h^{-6}$ . This is verified in Table 4, which presents the spectral radii of the more standard finite element approach proposed in [11]. Precisely, the scheme uses Gauss-Lobatto nodes and mass lumping, and results are presented for the smallest penalty parameter for which the spatial operator remains definite. The sixth order growth with p is clearly observed. Furthermore, for large p the spectral radius of the operators resulting from standard finite elements are observed to be orders of magnitude larger than the exact value  $\pi^6$  and the corresponding GD scheme.

## 3.3.3 Higher Order Operators

To further test the hypothesis of superconvergence at order 2p + 2 - 2m, we fix p = 11 and display below the symbols of the Galerkin Difference approximations for the m-th derivative



p	5	7	9	11	13
$\rho_{FEM}$	$6.4 \times 10^4$	$4.2 \times 10^{4}$	$1.8 \times 10^{5}$	5.6 × 10 <sup>5</sup>	$1.5 \times 10^{6}$
$ ho_{FEM}/\pi^6$	$6.7 \times 10^{0}$	$4.4 \times 10^{1}$	$1.8 \times 10^2$	$5.8 \times 10^{2}$	$1.6 \times 10^{3}$
$ ho_{GD}$	$4.6 \times 10^{2}$	$6.0 \times 10^{2}$	$6.8 \times 10^{2}$	$7.3 \times 10^{2}$	$7.7\times10^2$
$ ho_{FEM}/ ho_{GD}$	$1.4 \times 10^1$	$7.1 \times 10^{1}$	$2.6 \times 10^{2}$	$7.7 \times 10^{2}$	$2.0 \times 10^{3}$

**Table 4** Computed spectral radius  $\rho_{FEM}$  as a function of p for standard SIPGD approximations to the sixth derivative with periodic boundary conditions and Gauss-Lobatto nodes.

Here the element widths are H=p so the methods have the same grid average grid density as Galerkin Difference discretizations with h=1. The ratio  $\rho_{FEM}/\pi^6$  illustrates the growth in the spectral radius of the standard SIPGD scheme in relation to the continuous limit  $\pi^6$  (i.e. the Fourier derivative with two points per wavelength). Also included is the spectral radius of the GD method with periodic boundary conditions,  $\rho_{GD}$ . The ratio  $\rho_{FEM}/\rho_{GD}$  illustrates the improvement in spectral radius for GD vs. the standard SIPGD scheme

with m = 4, ..., 11

$$\begin{split} \mathcal{S}^{(8,11)} &= \eta^8 - \frac{445365299}{111929610240000} \eta^{24} + \frac{11060415400747}{3193183885731840000} \eta^{26} + O\left(\eta^{28}\right) \\ \mathcal{S}^{(10,11)} &= -\eta^{10} + \frac{560137}{6897623040} \eta^{24} - \frac{70317997643}{1067062284288000} \eta^{26} + O\left(\eta^{28}\right) \\ \mathcal{S}^{(12,11)} &= \eta^{12} - \frac{2140239721}{2615348736000} \eta^{24} + \frac{50653411}{79252992000} \eta^{26} + O\left(\eta^{28}\right) \\ \mathcal{S}^{(14,11)} &= -\eta^{14} + \frac{392251}{68428800} \eta^{24} - \frac{11204393537}{2615348736000} \eta^{26} + O\left(\eta^{28}\right) \\ \mathcal{S}^{(16,11)} &= \eta^{16} - \frac{11129}{362880} \eta^{24} + \frac{965}{44352} \eta^{26} + O\left(\eta^{28}\right) \\ \mathcal{S}^{(18,11)} &= -\eta^{18} + \frac{331}{2520} \eta^{24} - \frac{281}{3200} \eta^{26} + O\left(\eta^{28}\right) \\ \mathcal{S}^{(20,11)} &= \eta^{20} - \frac{61}{144} \eta^{24} + \frac{85}{336} \eta^{26} + O\left(\eta^{28}\right) \\ \mathcal{S}^{(22,11)} &= -\eta^{22} + \frac{11}{12} \eta^{24} - \frac{33}{80} \eta^{26} + O\left(\eta^{28}\right). \end{split}$$

Clearly the hypothesized convergence rate is supported by the data. Similar results can be obtained for other p, although the results are omitted here for brevity.

# 4 Boundary Conditions and Discrete Spectra

The previous section established the basic properties of the GD methods for periodic problems. Of note are the superconvergence of the dispersion errors, the stability without the need for penalty parameters, and the boundedness of the spectrum as the order is increased. Of practical importance is the extent to which these favorable properties are maintained in the presence of boundaries. Based on prior GD work, we do not necessarily expect that the methods will converge at double the design order in the presence of boundaries unless compatibility boundary closures are used, although, we do expect that small dispersion errors will allow accurate propagation over many wavelengths. In addition, we will demonstrate numerically that stability is maintained for the penalty-free formulation and, most impor-



tantly, that the growth of the eigenvalues with order is mild when we employ what are termed direct enforcement (DE) boundary closures.

## 4.1 Enforcement of Boundary Conditions

As in all GD schemes, closures must be applied near domain boundaries since the GD basis extends over multiple elements. The original approaches described in [14, 17] include extrapolation, ghost basis, and compatibility closures. All three make use of so-called *ghost points*, which can be viewed as degrees of freedom (DoFs) associated with points located outside the physical domain.<sup>2</sup> In the ghost basis closure these degrees of freedom are simply maintained with all other DoFs, and evolved according to the weak-form PDE. In extrapolation and compatibility closures, algebraic constraint equations are used to relate the DoFs in the ghost cells to the domain interior, and they are then eliminated from the system. This results in changes to the basis functions near boundaries and ultimately constrains the space of Galerkin Difference functions. In [14, 17], the compatibility closure was found to lead to superior results in terms of operator stiffness and observed global superconvergence, but the mechanics of the closure can be unwieldy, and the conditions may be difficult to derive and/or implement in some cases. This is particularly true for high-order operators, such as those under consideration here, and so in [16] a middle ground approach, deemed direct enforcement, was devised.

In the DE approach only the leading compatibility conditions, which are simply highorder accurate discrete representations of the physical boundary conditions, are imposed on the basis, and all other constraints are simply taken to be high-order extrapolation. DE closure will be adopted here, and is found to yield remarkably small growth in the spectral radius of the discretization matrix. For clarity a brief description of the approach is provided below. Also note that while not pursued herein, it may also be possible to use weak imposition of the boundary conditions, as is common in the standard interior penalty literature, e.g. [20, 22, 23]. However, preliminary testing for second order partial differential equations (not presented here) suggests that weak imposition can lead to larger spectral radii for the discretization matrices, which implies unwanted artificial stiffness. A full analysis of the effects of weakly imposed boundary conditions is left as a topic for further research.

To describe the DE approach, it is sufficient to consider a specific example, with extension to other boundary conditions being straightforward. Consider the fourth order derivative operator with a free boundary condition  $u_{xx}(x_0) = u_{xxx}(x_0) = 0$  on the left boundary at  $x = x_0$ . Now suppose that the GD discretization with p = 7 is used, which would require the specification or evolution of values at three ghost points. The DE-closure would impose three constraint equations which are given by centered finite difference discretizations of  $u_{xx}(x_0) = 0$  and  $u_{xxx}(x_0) = 0$  using a p-point stencil, and a single order p+1 extrapolation condition. Specifically these constraints are given by

$$\frac{1}{90}u_{-3} - \frac{3}{20}u_{-2} + \frac{3}{2}u_{-1} - \frac{49}{18}u_0 + \frac{3}{2}u_1 - \frac{3}{20}u_2 + \frac{1}{90}u_3 = 0$$
 (32a)

$$\frac{1}{8}u_{-3} - u_{-2} + \frac{13}{8}u_{-1} - \frac{13}{8}u_1 + u_2 - \frac{1}{8}u_{-3} = 0$$
 (32b)

$$-u_{-3} + 8u_{-2} - 28u_{-1} + 56u_0 - 70u_1 + 56u_2 - 28u_3 + 8u_4 - u_5 = 0$$
 (32c)

<sup>&</sup>lt;sup>2</sup> In fact the ghost DoFs describe aspects of the solution on the domain interior, but it is conceptually useful to think of them as living outside the domain.



where  $u_j = u^h(x_j)$ ,  $x = x_0 + jh$ . Here, Eq. (32a) specifies a finite difference approximation to the second derivative, Eq. (32b) specifies the third derivative, and Eq. (32c) specifies the extrapolation condition. All together (32) specifies three equations for the three unknown ghost points  $u_{-3}$ ,  $u_{-2}$ , and  $u_{-1}$  in terms of interior data. These constraints are applied to both the test and trial functions, and in practice are implemented by removing the DoFs from the discrete system. As shown in [16], the DE boundary closure leads to remarkably mild growth in the spectral radius and condition number of the complete derivative operator. Also note that for cases involving a displacement boundary condition u = 0, both the constraint  $u_0 = 0$  and an averaging operator with the same stencil as the difference operators are applied as constraint equations. In effect this implies a system of 4 equations in 4 unknowns for the p = 7 case. This approach is observed to yield superior performance in comparison to only imposing the averaging operator on the boundary. Finally note that the extension of the DE approach to higher-order derivative boundary conditions with high-order operators is straightforward.

One final point about boundary condition imposition is that two applications of integration by parts produces boundary terms in the weak-form operator, e.g.

$$BTs = -u_{xxx}(x_0)\phi(x_0) - u_{xx}(x_0)\phi_x(x_0), \tag{33}$$

where  $x_0$  is a point on the boundary. The DE closure does not directly enforce constraints on the derivatives and instead only enforces approximations to derivatives. Therefore, boundary terms, such as those in (33), should be included in the weak form discretization with values of the derivatives being defined by the underlying piecewise interpolant. Failure to do so may lead to reduced convergence rates.

As a specific experiment we consider the computed spectra for approximations to the fourth derivative operator on the interval (0, 10) with h = 0.1. Time-domain simulations using these operators will be shown in Sect. 5. Here we consider two cases corresponding to fixed and free boundary conditions:

$$u(0) = u_x(0) = 0, \quad u_{xx}(10) = u_{xxx}(10) = 0,$$
 (34)

and sliding and simply supported boundary conditions:

$$u_x(0) = u_{xxx}(0) = 0, \quad u(10) = u_{xx}(10) = 0.$$
 (35)

We first note that positivity without the imposition of penalty terms was maintained in these experiments. Normalized spectral radii as a function of p for the boundary condition (34) are shown in Table 5. It is also interesting to probe the stiffness of the discrete operator by comparing the spectral radius of the discretization matrix to the spectrum of the continuous operator restricted to wave numbers supported on the grid. For the lower order methods, p=5 and p=7, the discretization is somewhat less stiff than the continuous problem, while for higher order methods the spectral radius grows moderately. The growth for the present scheme is slightly more severe than the growth observed for the GD-DSpline scheme in [16]. However, a comparison with Table 2 shows that the growth is much milder than what we observe for standard elements and periodic boundary conditions. Note also that the spectral radius of the discrete operator for this computation is dominated by the free boundary condition.

Results for boundary conditions (35), displayed in Table 6, are similar. Here the spectral radius of the discrete operator is dominated by the simply supported boundary. As the order of accuracy increases, the simply supported and sliding boundary conditions are generally less stiff than those of the fixed and free case due to the fact that the free boundary condition introduces the most artificial stiffness among the set considered.



**Table 5** Normalized spectral radii,  $\rho^{(p)}h^4/\pi^4$ , of the discretized operators for various p using N=100 for the fixed and free boundary conditions

p	5	7	9	11	19
$\rho^{(p)}h^4/\pi^4$	.8484	.8976	1.6981	2.2901	8.0137
n	5	7	9	11	19

8998

1.5625

2.6562

5.3146

**Table 6** Normalized spectral radii of the discretized operators with N=100 for the simply supported and sliding boundary conditions at various orders p,  $\rho^{(p)}h^4/\pi^4$ 

## 4.2 Extension to Complex Domains

In the experiments shown below we restrict attention to simple domains. However, though beyond the scope of the current work, we emphasize that it is straightforward to apply the Galerkin Difference discretizations in more complex settings using the techniques described in [17, 18]. Specifically, we would use multiblock mapped grids, which can simply be viewed as large macroelements, possibly combined with small unstructured grid components where the methods proposed in [10, 11] could be applied. As each grid component can be simply viewed as a (possibly quite large) element, fluxes across interelement boundaries follow directly from the weak formulation. (It is possible that penalty parameters would have to be introduced at these boundaries.) Of course if unstructured grid components are employed it could be advantageous to use some local time stepping strategy to overcome the artificial stiffness of the standard SIPGD elements at high order.

8496

 $o^{(p)}\Delta x^4/\pi^4$ 

To be concrete, consider a mapping x = X(r, s), y = Y(r, s) with (r, s) residing in a rectangular reference domain. Derivatives and integrals appearing in the weak form are simply expressed in the (r, s) coordinates where the Galerkin Difference space is defined as before. The procedure is completely analogous to the use of reference elements in standard finite element constructions. In this case, and for problems with variable coefficients in general, the mass and stiffness matrices remain banded but lose the tensor-product structure. For implicit time stepping schemes and the direct solver used in the numerical experiments below this would not lead to increased complexity, though we could have developed specialized fast solvers exploiting the matrix structure in our simple cases.

# 5 Application to the Euler-Bernoulli Beam and Kirchoff-Love Plate

As a physically motivated application of the proposed Galerkin Difference approximations to PDEs with high order derivative operators, consider the time evolution of thin solid bodies. In particular, the linear (infinitesimal) deflection of a one-dimensional solid beam or two-dimensional solid plate is governed by

$$\rho u_{tt} = -\nabla^2 \left( D \nabla^2 u \right), \tag{36}$$

where u is the displacement of the beam,  $\rho$  is the density, and D > 0 is the flexural rigidity. In one space dimension, this is the Euler-Bernoulli beam equation, and in two space dimensions, this is the Kirchoff-Love plate equation. At any point along the physical boundary of the



domain, two boundary conditions are required; typically two conditions from among the displacement and the first through third derivatives are specified.

It will suffice to provide a detailed description of the scheme and boundary closures in 1D, with extension to multiple space dimensions being accomplished using tensor product basis functions as in [15–17]. Using the symmetric interior penalty Galerkin Difference approach, the variational form corresponding to (36) in one space dimension is given by

$$\int_{\Omega} \rho u_{tt} \phi dx = -\int_{\Omega} D u_{xx} \phi_{xx} - D \sum_{k} [\{\{u_{xx}\}\} [\![\phi_{x}]\!] + [\![u_{x}]\!] \{\{\phi_{xx}\}\}]_{x=x_{k}} + BTs, \quad (37)$$

where BTs refers to boundary terms occurring at the physical boundary of the domain; these will be discussed in the next section. Equation (37) can be rewritten in matrix form as

$$\rho M^{(p)} \mathbf{u}_{tt}^{h} = D(K^{(4,p)} + F^{(4,p)}) \mathbf{u}^{h} + BTs, \tag{38}$$

where the coefficients of the mass matrix  $M^{(p)}$ , the stiffness matrix  $K^{(4,p)}$ , and the lift matrix  $F^{(4,p)}$  are given, for example, in Table 1 for the case of p=3. For standard  $C^0$  finite element spaces, Eq. (37) must be augmented by including appropriate penalty terms to ensure coercivity, and was analyzed in [22]. However, due to the unique features of the Galerkin Difference space used here, stability of (37) is ensured without the need for additional penalty terms, see Theorem 1, and the analysis of [22] can therefore be applied directly to (37). Furthermore, the dispersion analysis in Sect. 3.3.1 demonstrates that away from the boundary, a nodal superconvergence is expected, and will be observed for the  $\ell^2$  norm.

## 5.1 Spectral Deferred Correction Time Stepping Scheme

For the sake of completeness, the time stepping scheme used to generate numerical results is now briefly discussed. The method, and discussion, follow closely from [16, 24]. Due to the fact that the eigenvalues of the bi-harmonic operator grow as  $\sim h^{-4}$ , explicit time stepping of the discrete form of (36) will lead to a time step restriction  $\Delta t \propto h^2$ , and it is therefore natural to consider implicit time discretizations that may enable larger time steps, e.g.  $\Delta t \propto h$ . To leverage the large body of existing work for implicit time integration, consider the first-order-in-time formulation Eq. (36)

$$\begin{bmatrix} u \\ v \end{bmatrix}_t = \begin{bmatrix} v \\ -\nabla^2 (D\nabla^2 u) \end{bmatrix} = \begin{bmatrix} 0 & 1 \\ \mathcal{L} & 0 \end{bmatrix} \begin{bmatrix} u \\ v \end{bmatrix}, \tag{39}$$

where  $\mathcal{L}u \equiv -\nabla^2(D\nabla^2u)$ , and  $v=u_t$  can be considered the velocity of the beam. Since the RHS of (36) is a negative definite operator, the equivalent first-order temporal formulation (39) will have purely imaginary eigenvalues. Furthermore, the proposed GD scheme will retain these properties, and so to ensure a favorable stability time step restriction such as  $\Delta t \propto h$ , the integration scheme should be A-stable. In addition, high temporal accuracy is required so that the observed accuracy in numerical computations will be that of the spatial operator rather than that of the time-stepping scheme. To that end, a Spectral Deferred Correction (SDC) time stepping scheme is used.

Precisely, we employ here a backward Euler-like method<sup>3</sup> in a defect correction iteration that ultimately yields a high-order accurate result. As is typical in method-of-lines formulations, after spatial discretization all degrees of freedom are arranged into a vector

<sup>&</sup>lt;sup>3</sup> We use the term "backward Euler-like" since at its core the low-order scheme is actually a discretization of a Picard integral formulation, although the resulting scheme may be identical to backward-Euler.



of unknowns, here called y, and the associated ODE system can be succinctly expressed  $\mathbf{y}' = \mathbf{A}\mathbf{y}$ , where **A** is the discretization matrix. Note that at present we employ direct methods to solve the linear system required to form Ay, although it may be possible to take advantage of the Kronecker structure for increased efficiency.

Temporal integration starting from  $t = t_n$  with initial condition  $\mathbf{y}(t_n) = \mathbf{y}_n$  yields the Picard formulation of the ODE system

$$\mathbf{y}(t) = \mathbf{y}_n + \int_{t_n}^t \mathbf{A} \mathbf{y}(\tau) \, d\tau. \tag{40}$$

We approximate the integral by a Gauss-Radau scheme and carry out the standard SDC interations with the backward Euler method used to compute the defect corrections. For the computations to follow, we take 10 Gauss-Radau nodes and 30 correction steps, which yields a 19-th order accurate A-stable time integration scheme; see [16].

#### 5.2 Numerical Results for the Euler Bernoulli Beam

To demonstrate properties of the proposed numerical method, we adopt similar tests to those presented in [16]. Because the same test cases are simulated with the same grid parameters, direct comparison of the two methodologies is possible. To that end, consider the solution to Eq. (36) in one space dimension with  $\rho = D = 1$  on the domain  $x \in (0, L)$  and boundary conditions to be specified in the coming example computations. To derive exact solutions, assume separable solutions of the form u(x, t) = g(t) f(x). Substitution into the PDE then yields

$$f_{xxxx} - \lambda^4 f = 0, (41)$$

where  $\lambda$  is the constant from separation of variables and f satisfies the same boundary conditions as u(x, t) at x = 0, L. Upon specification of BCs, the spatial eigenfunctions are determined, and subsequently the exact solution can be found. For additional details of the derivation refer to [16]. Details of the various exact solutions are given as the test cases are presented in the following subsections. In what follows, all of the reported errors are computed in the  $\ell^2$  norm,  $\|u\|_{\ell^2_h} = \sqrt{\frac{1}{h} \sum_{i \in \mathbf{j}} u_i^2}$ , and all time stepping is done using the previously described SDC scheme

## 5.2.1 Cantilever Beam (Fixed and Free Boundary Conditions)

First consider the classical case of a cantilever beam that is affixed at the left end and free at the right end. The boundary conditions describing this situation are  $u(0, t) = u_x(0, t) = 0$ and  $u_{xx}(L,t) = u_{xxx}(L,t) = 0$ . Taking L = 10, and  $\lambda = .65\pi$ , one can use separation of variables to give an exact solution as

$$u(x,t) = \cos(\lambda^2 t) \left(\cos(\lambda x) - \cosh(\lambda x) + S \left(\sinh(\lambda x) - \sin(\lambda x)\right)\right),\tag{42}$$

where  $S \approx 0.999999972924051$ , a value correct up to the limitations of double precision. For reference, the initial condition is plotted in Fig. 4, and the solution simply oscillates as a standing wave with increasing time. As in [16], numerical approximations of the solution are computed to a final time  $t_f = 3$ , a time which does not correspond to a node or anti-node of the standing-wave oscillation.

Results will be presented for the GD scheme with p = 5:2:13. Note that the notation a: s: b is MATLAB-style for a list starting at a and incrementing by s to b. Convergence



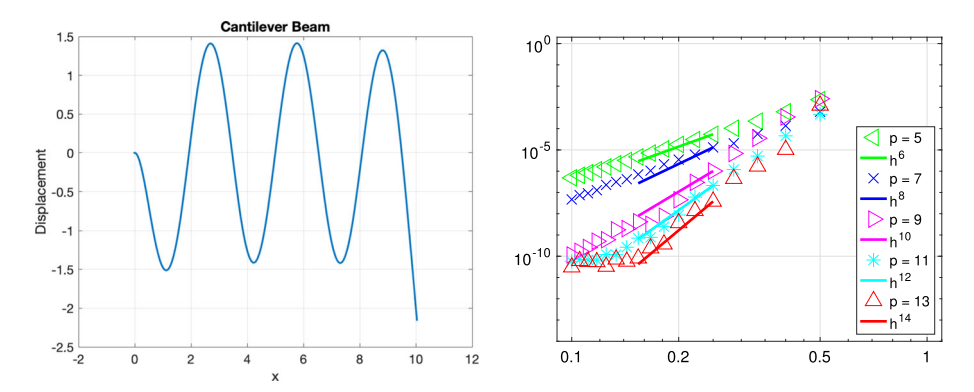


**Fig. 4** Left: Initial condition for cantilever beam. Right: Convergence study for various order schemes defined by p as well as reference lines indicating  $\mathcal{O}(h^{p+1})$ 

results are shown in Fig. 4 for N=20:5:100 with h=L/N. While the dispersion error analysis of Sect. 3.3 indicates that the error for the domain interior is  $\mathcal{O}(h^{2p-2})$  for degree p basis functions, the finite difference stencil for the 3rd derivative used in the direct enforcement boundary closure has error  $\mathcal{O}(h^{p-3})$ , and a reduction in error is therefore expected. The observed convergence rate in Fig. 4 is rather close to  $\mathcal{O}(h^{p+1})$ , as indicated by the reference lines. This rate is consistent with the prediction for energy stable finite difference schemes, as presented in [25], assuming certain conditions on the null space of the difference operators hold. We believe these follow from our direct enforcement boundary closures, but we do not have a general proof. In addition, comparison of the errors presented here to those shown in [16] reveal that the two schemes' behavior is very similar, although the present scheme has relaxed the requirements of  $C^1$  continuity, and is therefore arguably simpler to implement.

#### 5.2.2 Simply Supported and Sliding Boundary Conditions

Now consider a beam with sliding and simply supported boundary conditions, i.e.  $u_x(0, t) = u_{xxx}(0, t) = 0$  and  $u(L, t) = u_{xx}(L, t) = 0$ . Again taking L = 10 and  $\lambda = .65\pi$ , the exact solution is

$$u(x,t) = \cos(\lambda^2 t)\cos(\lambda x). \tag{43}$$

Figure 5 shows the initial condition, as well as convergence results at  $t_f = 3$  for N = 20:5:100 with h = L/N. Similar to the previous case, a reduction of order from the dispersion analysis is Sect. 3.3 is expected due to the use of lower-order accurate finite difference stencils in the direct enforcement boundary closure. As before, convergence rates of  $\mathcal{O}(h^{p+1})$  are observed in all cases except p = 5. It is likely that this is simply fortuitous, since the solution consists of pure sinusoids for which the two direct enforcement boundary closure equations for p = 5 are in fact spectrally accurate. As a result, for this test case the superconvergent  $\mathcal{O}(h^{2p-2})$  is observed. For higher p, the addition of extrapolation equations at the boundary disrupts this behavior. In comparing the present results to those from the GD D-Spline formulation in [16], we observe comparable accuracy aside from the fortuitously accurate p = 5 case.



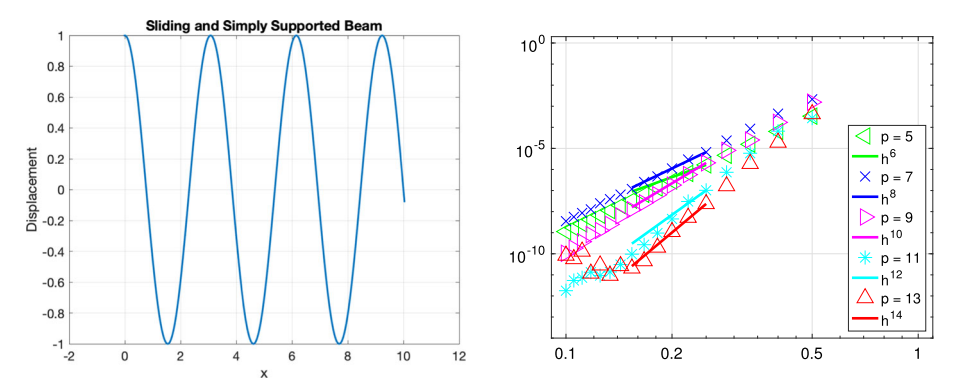


Fig. 5 Left: Initial condition for a beam with simply supported boundary at x = 0 and sliding boundary at x = L. Right: Convergence study for various order schemes defined by p as well as reference lines indicating  $\mathcal{O}(h^{p+1})$ 

#### 5.3 Numerical Results for Kirchhoff-Love Plate

Exact solutions for the 2D Kirchhoff-Love plate are often more difficult to express in closed form than are those of the 1D beam equations. Nevertheless, for certain combinations of boundary conditions, the eigenfunctions remain sinusoids (similar to the case of simple and sliding BCs in Sect. 5.2.2), and these cases therefore make sensible numerical tests. For example consider the case of a 2D plate that is simply supported on two adjoining sides and sliding on the other two adjoining sides. The boundary conditions for this case are given by

$$u(x,0) = u_{yy}(x,0) = 0 (44a)$$

$$u_x(0, y) = u_{xxx}(0, y) = 0$$
 (44b)

$$u(L, y) = u_{xx}(L, y) = 0$$
 (44c)

$$u_{\nu}(x, L) = u_{\nu\nu\nu}(x, L) = 0,$$
 (44d)

where here the size is taken to be  $L = 9\pi/2$ . In this case the exact solution is given by

$$u(x, y, t) = \cos(k_x x)\sin(k_y y)\cos((k_x^2 + k_y^2)t),$$
(45)

where  $k_x$  and  $k_y$  are constrained to be odd integers. Here we take  $k_x = k_y = 1$  (initial conditions shown in Fig. 6), and integrate to a final time  $t_f = 3$ . Computations are performed for p = 5:2:13, and grid resolutions defined by  $N_x = N_y = 10:5:50$ . The results of the  $\ell^2$  convergence study are shown in Fig. 6. The results for p=7:2:14 exhibit convergence at the  $\mathcal{O}(h^{p+1})$  rate, as predicted by the analysis in [25] and observed in Sects. 5.2.1 and 5.2.2. Furthermore, similar to the results presented in Sect. 5.2.2, the case of p = 5 appears to exhibit fortuitous convergence. This is again attributed to symmetry in the exact solution leading to spectrally accurate difference formulas in the Direct Enforcement boundary closure, and ultimately to the observed superconvergent rate  $\mathcal{O}(h^{2p-2})$ . As a simple check, Fig. 7 shows the computed error at the final time  $t_f = 50$  for p = 5 and p = 9 using  $N_x = N_y = 50$ . In that figure, the case of p=5 produces an error that is clearly smooth, and qualitatively resembles the eigenfunction and exact solution. Such a situation is expected to lead to convergence as predicted by the dispersion error analysis of Sect. 3.3, which is consistent with the observed convergence. On the other hand for p = 9, the error is rough and the largest errors are observed near the boundaries. This is the result of broken symmetries imposed by the extrapolation



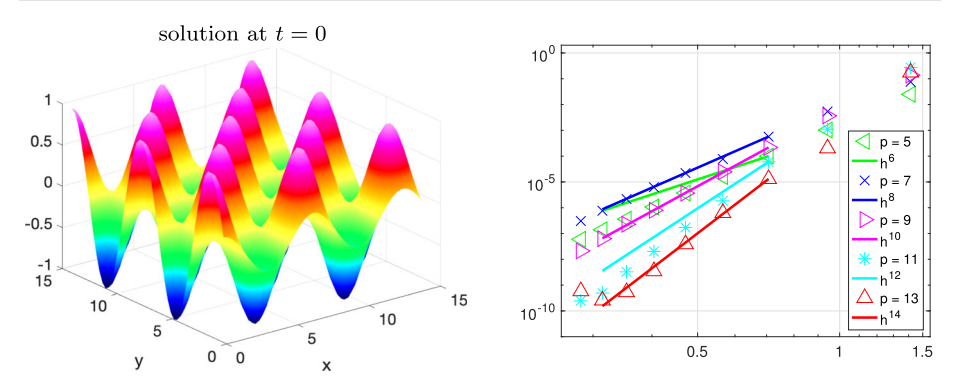


**Fig. 6** Left: Eigenfunction and initial condition for the 2D Kirchhoff-Love plate with sliding supports at left and top, and simple supports at right and bottom. Right: Convergence study for Kirchhoff-Love plate using p = 5:2:13, and grid resolutions defined by  $N_x = N_y = 10:5:50$ 

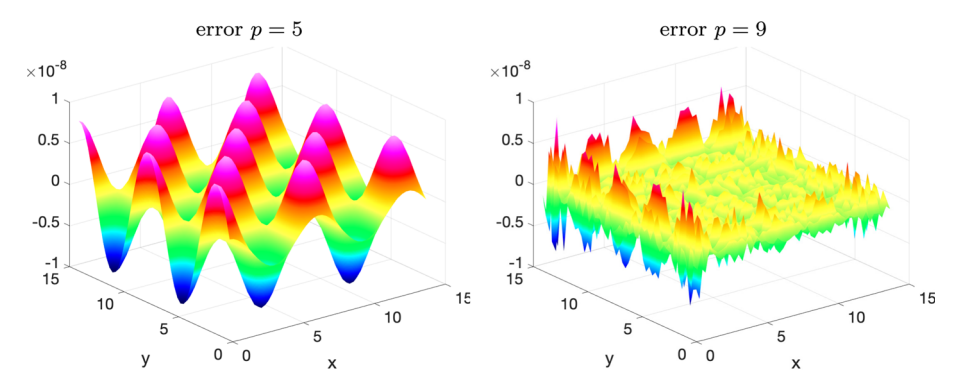


**Fig. 7** Left: Error in computed approximation with p = 5 and  $N_x = N_y = 50$  at  $t_f = 3$ . Right: Error in computed approximation with p = 9 and  $N_x = N_y = 50$  at  $t_f = 3$ . For p = 5 the error is clearly smooth, and qualitatively resembles the eigenfunction and exact solution (see Fig. 6). For p = 9 the error is rough and largest near the boundaries; a result of symmetries being broken by the extrapolation condition in the boundary closure

condition in the boundary closure. In this case then the dispersion error analysis of Sect. 3.3 would indicate small truncation error on the domain interior. There would be larger errors near the boundaries due to the DE closure, and the analysis in [25] would indicate  $\mathcal{O}(h^{p+1})$ , again consistent with the observation.

## **6 Conclusions**

In conclusion, we have developed a general approach for constructing coercive Galerkin Difference approximations to even order differential operators using a symmetric interior penalty formulation. Superconvergence of the discrete dispersion relation is demonstrated as well as optimal-order convergence for some standard fourth order problems arising as models of beams and plates.

Future directions for this research include the development of analogous discretizations of odd order derivatives and applications to problems in more complex geometry using mapped



grid blocks and/or hybrid structured-unstructured grids. These are demonstrated in [18] for Galerkin Difference discretizations of first order hyperbolic systems.

Funding J.W. Banks and B. Brett Buckner were supported in part by contracts from the U.S. Department of Energy ASCR Applied Math Program, and by a U.S. Presidential Early Career Award for Scientists and Engineers. T. Hagstrom was supported in part by NSF Grant DMS-2012296. Any opinions, findings, and conclusions or recommendations expressed in this material are those of the authors and do not necessarily reflect the views of the National Science Foundation.

Data Availability The data generated during and/or analysed during the current study are available from the corresponding author upon reasonable request.

#### Declarations

**Competing interests** The authors have no relevant financial or non-financial interests to disclose.

## References

- 1. Meirovitch, L.: Analytical Methods in Vibrations. MacMillan, New York (1967)
- 2. Boussinesq, J.: Théorie des ondes et des remous qui se propagent le long d'un canal rectangulaire horizontal, en communiquant au liquide contenu dans ce canal des vitesses sensiblement pareilles de la surface au fond. J. Math. Pures Appl. 17, 55 (1872)
- 3. Korteweg, D.J., de Vries, G.: XLI. On the change of form of long waves advancing in a rectangular canal, and on a new type of long stationary waves. The London, Edinburgh, and Dublin Philosophical Magazine and Journal of Science 39(240), 422 (1895)
- 4. Wazwaz, A.M.: Exact solutions for the fourth order nonlinear Schrodinger equations with cubic and power law nonlinearities. Math. Comput. Model. 43(7–8), 802 (2006)
- 5. Timošenko, S.P., Woinowsky-Krieger, S.: Theory of Plates and Shells, 2nd edn. Engineering Societies Monographs, McGraw-Hill, New York (1987)
- 6. Argyris, J.H., Fried, I., Scharpf, D.W.: The TUBA Family of Plate Elements for the Matrix Displacement Method. Aeronaut. J. **72**(692), 701 (1968)
- 7. Cheng, X.L., Han, W., Huang, Hc.: Some mixed finite element methods for biharmonic equation. J. Comput. Appl. Math. **126**(1–2), 91 (2000)
- 8. Monk, P.: A Mixed Finite Element Method for the Biharmonic Equation. SIAM J. Numer. Anal. 24(4), 737 (1987)
- 9. Brenner, S.C., Scott, L.R.: The Mathematical Theory of Finite Element Methods. In: Texts in Applied Mathematics, vol. 15. Springer, New York, NY (1994)
- 10. Engel, G., Garikipati, K., Hughes, T.J.R., Larson, M.G., Mazzei, L., Taylor, R.L.: Continuous/discontinuous finite element approximations of fourth-order elliptic problems in structural and continuum mechanics with applications to thin beams and plates, and strain gradient elasticity. Comput. Methods Appl. Mech. Engrg. 191, 3669 (2002)
- 11. Gudi, T., Neilan, M.: An interior penalty method for a sixth-order elliptic equation. IMA J. Num. Anal. **31**, 1734 (2011)
- 12. Cao, W., Huang, Q.: Superconvergence of local discontinuous Galerkin methods for partial differential equations with higher order derivatives. J. Sci. Comput. 72, 761 (2017)
- 13. Cao, W., Zhang, Z.: Some recent developments in superconvergence of discontinuous Galerkin methods for time-dependent partial differential equations. J. Sci. Comput. 77, 1402 (2018)
- 14. Banks, J., Hagstrom, T.: On Galerkin difference methods. J. Comput. Phys. 313, 310 (2016)
- 15. Banks, J.W., Buckner, B.B., Hagstrom, T., Juhnke, K.: Discontinuous-Galerkin Galerkin-Differences for the Wave Equation in Second-Order Form. SIAM J. Sci. Comput. 43, A1497 (2021)
- 16. Jacangelo, J., Banks, J.W., Hagstrom, T.: Galerkin Differences for High-Order Partial Differential Equations. SIAM J. Sci. Comput. 42, B447 (2020)
- 17. Banks, J., Hagstrom, T., Jacangelo, J.: Galerkin Differences for acoustic and elastic wave equations in two space dimensions. J. Comput. Phys. 372, 864 (2018)
- 18. Kozdon, J., Wilcox, L., Hagstrom, T., Banks, J.: Robust approaches to handling complex geometries with Galerkin difference methods. J. Comput. Phys. **392**, 483 (2019)



- Hagstrom, T., Banks, J.W., Buckner, B.B., Juhnke, K.: Discontinuous Galerkin Difference methods for symmetric hyperbolic systems. J. Sci. Comput. 81, 1509 (2019)
- Rivière, B., Wheeler, M.: Discontinuous finite element methods for acoustic and elastic wave problems. Contemp. Math. 329, 271 (2003)
- Strikwerda, J.: Finite Difference Schemes and Partial Differential Equations. Society for Industrial and Applied Mathematics, Philadelphia, PA (2004)
- Süli, E., Mozolevski, I.: hp-version interior penalty DGFEMs for the biharmonic equation. Comput. Methods Appl. Mech. Engrg. 196(13–16), 1851 (2007)
- Rivière, B.: Discontinuous Galerkin Methods For Solving Elliptic And Parabolic Equations: Theory and Implementation. Society for Industrial and Applied Mathematics, Philadelphia, PA, USA (2008)
- Dutt, A., Greengard, L., Rokhlin, V.: Spectral deferred correction methods for ordinary differential equations. BIT 40, 241 (2000)
- Svärd, M., Nordström, J.: On the convergence rates of energy-stable finite-difference schemes. J. Comput. Phys. 397, 108819 (2019)

**Publisher's Note** Springer Nature remains neutral with regard to jurisdictional claims in published maps and institutional affiliations.

